Rare Metal Materials and Engineering
Volume 53, Issue 10, October 2024
Available online at www.rmme.ac.cn

Science Press

Cite this article as: Zhang Yuezhong, Chen Xiaoting, Shen Jing, et al. Effects of Cu on Microstructure and Corrosion Behaviour of Hot-Rolled Mg-3Zn-1Y Alloys[J]. Rare Metal Materials and Engineering, 2024, 53(10): 2794-2804. DOI: 10.12442/j.issn.1002-185X.20240299.

ARTICLE

Effects of Cu on Microstructure and Corrosion Behaviour of Hot-Rolled Mg-3Zn-1Y Alloys

Zhang Yuezhong[1], Chen Xiaoting[1], Shen Jing[1], Wu Pengpeng[2], Zhang Shaohua[2], Liu Baosheng[2]

[1] College of Chemical Engineering and Technology, Taiyuan University of Science and Technology, Taiyuan 030024, China; [2] College of Materials Science and Engineering, Taiyuan University of Science and Technology, Taiyuan 030024, China

Abstract: The microstructure and corrosion behaviour of hot-rolled Mg-3Zn-1Y-*x*Cu alloys (*x*=0, 1, 3, 5, wt%) were investigated. Results show that all Mg-3Zn-1Y-*x*Cu alloys mainly consist of α-Mg matrix and Mg_3Zn_6Y phases. The addition of Cu element promotes the formation of MgZnCu phase, and the amount of MgZnCu phase is increased with the increase in Cu content. Electrochemical and immersion test results show that the corrosion resistance of Mg-3Zn-1Y-*x*Cu alloys is deteriorated after Cu addition, which can be attributed to the influence of the microstructure of alloys and the properties of the formed corrosion product film. The MgZnCu phase with high electrochemical potential accelerates the micro-galvanic corrosion as strong cathodic sites, and the decreased protection effect of the corrosion product film results from the variation in PBR value of the related compounds.

Key words: corrosion behaviour; magnesium alloy; microstructure; MgZnCu phase; corrosion product

Mg-based alloys, as the lightest metal structural materials, have been widely used in electronics, automotive, and aerospace industries due to their excellent properties[1–4]. Unfortunately, the extensive and high-end application of Mg-based structural materials is severely restricted owing to their poor corrosion resistance. Consequently, much attention has been focused on corrosion resistance improvement through alloying technique. Among various alloying elements, Fe, Cu, and Ni elements are considered as impurity elements because they have a significant acceleration effect on the corrosion rate of Mg-based alloys[5–7]. Therefore, the purification of Mg alloys by reducing impurity elements (Fe, Cu, Ni) has attracted more and more attention. However, the corrosion nature of Mg alloys via alloying is rarely applied.

Recently, degradable plugging materials used in the oil and gas industry widen the application potential for the Mg alloys containing impurity elements. To satisfy the requirements of degradable materials, Cu element is added to the Mg alloys to increase strength and accelerate corrosion[8–11]. Besides, the effects of Cu addition on the microstructure and corrosion performance of Mg-Al, Mg-Zn, and Mg-Al-Zn (AZ) series alloys have been investigated[12–15]. For instance, Lotfpour et al[12] reported that the second phase of as-cast Mg-2Zn-*x*Cu alloy played an important role in the corrosion behaviour. Zhou et al[13] revealed that the accelerated corrosion rate of AZ31-*x*Cu alloy is attributed to the micro-galvanic corrosion between the AlCuMg phase cathode and the Mg matrix anode. It is well known that the corrosion accelerates dramatically once the impurity content exceeds the tolerance limit[7]. However, Safari et al[14] showed that Mg-1Al-0.25Cu alloy exhibited the smaller degradation rate than pure Mg and Mg-1Al alloy due to uniformly distributed fine Al_2Cu precipitates at the grain boundaries. Moreover, Xiao et al[15] reported that the corrosion rate of Mg-17Al-3Zn alloy is initially increased with the increase in Cu content from 0wt% to 0.5wt% and then decreased with the further increase in Cu content. When the Cu addition amount was 5wt%, the corrosion rate increased significantly. Therefore, the effects of Cu on the corrosion behaviour of different Mg alloys have significant differences.

Received date: May 17, 2024
Foundation item: Fundamental Research Program of Shanxi Province (202203021222188, 202303021211166); Central Guiding Science and Technology Development of Local Fund (YDZJSK20231A046); Key Scientific Research Project in Shanxi Province (202102050201003, 202203D111001)

Corresponding author: Zhang Yuezhong, Ph. D., Associate Professor, College of Chemical Engineering and Technology, Taiyuan University of Science and Technology, Taiyuan 030024, P. R. China, Tel: 0086-351-6998186, E-mail: yuezhongzhang@tyust.edu.cn

Recently, Mg-Zn-Y series alloys have attracted extensive attention because of their high mechanical properties[16–17], and they can be easily achieved by regulating the Zn/Y ratio[18–19]. Moreover, the Mg-Zn-Y series alloys are considered as a promising choice as basic materials for degradable application due to their high mechanical properties[20–21]. However, the effects of Cu on the corrosion behaviour of Mg-Zn-Y series alloys are rarely investigated, specifically for the deformed Mg alloy. Thus, the effect of Cu on the microstruture and corrosion behaviour of hot-rolled Mg-3Zn-1Y alloy was investigated in this research.

1 Experiment

Hot-rolled Mg-3Zn-1Y-*x*Cu (*x*=0, 1, 3, 5, wt%) alloys were used in this research. The alloy ingots were prepared by furnace melting of high-purity magnesium (99.99wt%), pure copper (99.95wt%), pure zinc (99.95wt%), and Mg-30Y master alloys. The materials were melted in a mild steel crucible with protective RJ-2 flux at 750 °C. The molten alloy was poured into a pre-heated cylindrical steel mould at 250 °C to produce billets with size of *Φ*90 mm×120 mm. After homogenization treatment at 400 °C for 24 h in a vacuum tube furnace, the ingot was extruded directly into plates with size of 44 mm (width)×11 mm (thickness) at 310 °C under the extrusion ratio of 16:1. Then, the extruded plates were rolled at 350 °C to form plates with size of 60 mm (width)×8 mm (thickness) in 2 passes (approximately 15% reduction per pass). Before each rolling pass, the plates were reheated for 20 min.

The microstructure of the Mg-3Zn-1Y-*x*Cu alloys was characterized by optical microscope (OM), scanning electron microscope (SEM, Hitachi S-4800) coupled with energy dispersive spectrometer (EDS), and transmission electron microscope (TEM, JEM-F200). Selected area electron diffraction (SAED) was also employed for analysis. The phase composition of Mg-3Zn-1Y-*x*Cu alloys was tested by X-ray diffractometer (XRD, Rigaku D/MAX-2500). The chemical composition of the corrosion product was analyzed by X-ray photoelectron spectroscope (XPS, Thermoelectron ESCALAB 250).

The corrosion behaviour was investigated by immersion and electrochemical tests in 3.5wt% NaCl solution at 25 °C. Before measurements, the samples were ground successively by sandpaper from 200# to 1200#, then ultrasonically cleaned in anhydrous alcohol and distilled water, and finally dried with air. The immersion test was performed according to G31-72 ASTM standard. Afterwards, the corrosion products were removed with 200 g/L Cr_2O_3 solution and the mass loss of the samples was measured.

The electrochemical tests were conducted by RST5000 electrochemical workstation with a three-electrode system, where Mg-3Zn-1Y-*x*Cu alloys serve as working electrodes, the Ag/AgCl electrode serves as the reference electrode, and the platinum plate serves as the auxiliary electrode. The open circuit potentials (OCPs) of Mg-3Zn-1Y-*x*Cu alloys in the corrosive medium were monitored for 30 min. Polarization curves were measured from −0.3 V vs. OCP to 0.3 V vs. OCP with the scanning rate of 0.5 mV/s. Electrochemical impedance spectroscopy (EIS) measurements were conducted in the frequency range of 10^5 – 10^{-2} Hz with a sinusoidal amplitude of 10 mV. Each electrochemical test was performed at least three times to ensure the reproducibility.

2 Results

2.1 Microstructures and composition of Mg-3Zn-1Y-*x*Cu alloys

XRD patterns of the hot-rolled Mg-3Zn-1Y-*x*Cu (*x*=0, 1, 3, 5) alloys are shown in Fig.1. For the Mg-3Zn-1Y alloy, *α*-Mg (major phase) and Mg_3Zn_6Y phases can be detected, which is consistent with the phase diagram[22] and the results in Ref. [23]. After alloying with Cu element, MgZnCu phases (JCPDS card No: 41-0778) can be detected as the major phase in the Cu-containing alloys. Clearly, the Mg_3Zn_6Y phase exists in all Cu-containing alloys, whereas the $Mg_3Zn_3Y_2$ phase can only be detected in Mg-3Zn-1Y-3Cu and Mg-3Zn-1Y-5Cu alloys.

Fig. 2 presents OM images of the hot-rolled Mg-3Zn-1Y-*x*Cu (*x*=0, 1, 3, 5) alloys. The average grain sizes of *α*-Mg matrix in Mg-3Zn-1Y-*x*Cu alloys with *x*=0, 1, 3, and 5 are 6.7±1.0, 4.8±0.6, 4.4±0.5, and 4.1±0.4 μm, respectively. The average grain size of the alloys decreases slightly after Cu addition, but it does not change significantly with the further increase in Cu content. Fig.3a–3d present SEM images of the hot-rolled Mg-3Zn-1Y-*x*Cu (*x*=0, 1, 3, 5) alloys embedded wtih different second phase particles. Most second phase particles can be observed at the grain boundary of the *α*-Mg matrix, and a small number of second phase particles exist in the *α*-Mg. Furthermore, the quantity of second phase particles increases significantly after Cu addition. The element composition of the second phase particles was analyzed by EDS and the results are shown in Table 1. The second phases in Cu-containing alloys show a similar element composition. The ratio of Mg: Zn: Cu is approximately 1: 1: 1, which confirms the existence of MgZnCu phase. To further identify the MgZnY phase, the second phase particles in the Mg-3Zn-1Y-5Cu alloy were investigated by TEM, as shown in Fig.3e

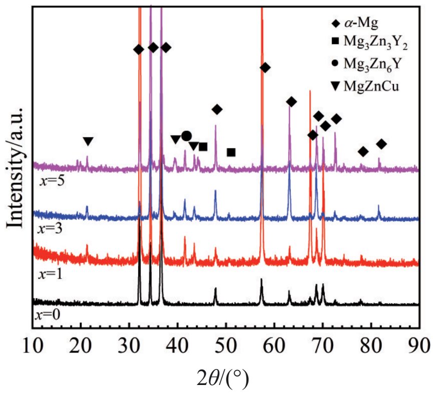

Fig.1 XRD patterns of Mg-3Zn-1Y-*x*Cu (*x*=0, 1, 3, 5) alloys

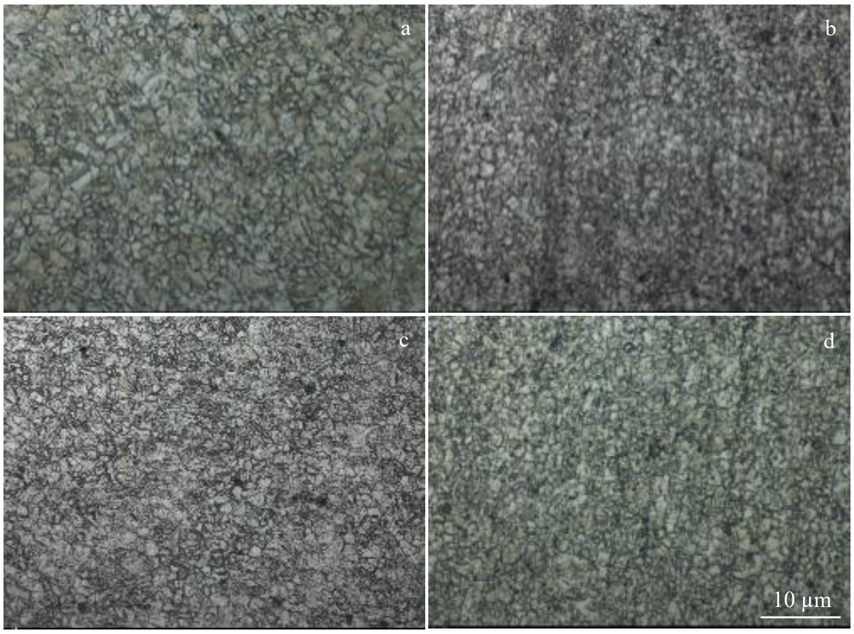

Fig.2 OM images of hot-rolled Mg-3Zn-1Y-*x*Cu alloys: (a) x=0, (b) x=1, (c) x=3, and (d) x=5

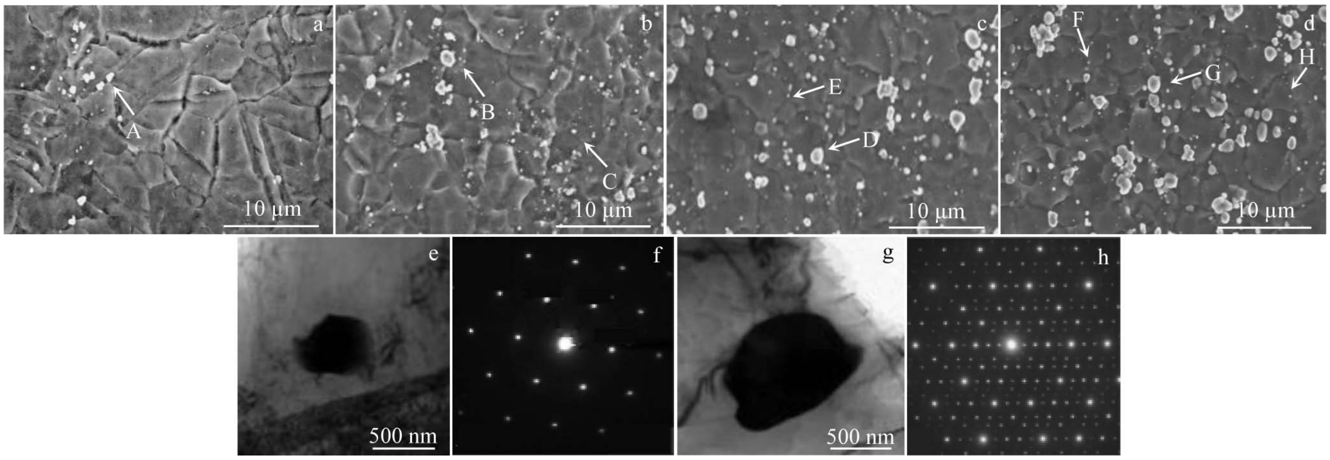

Fig.3 SEM images of hot-rolled Mg-3Zn-1Y-*x*Cu alloys: (a) x=0, (b) x=1, (c) x=3, and (d) x=5; TEM image (e) and corresponding SAED pattern along $[\bar{1}11]$ zone axis (f) of $Mg_3Zn_3Y_2$ particle; TEM image (g) and corresponding SAED pattern along 5-fold zone axis (h) of Mg_3Zn_6Y particle

Table 1 EDS analysis results of the second phase particles marked in Fig.3

Location	x	Phase	Element content/at%			
			Mg	Zn	Y	Cu
A	0	Mg_3Zn_6Y	32.2	58.6	9.2	-
B	1	Mg_3Zn_6Y	31.7	58.8	9.5	-
C	1	MgZnCu	34.9	31.6	-	33.5
D	3	Mg_3Zn_6Y	29.6	60.6	9.8	-
E	3	MgZnCu	35.2	33.1	-	32.7
F	5	$Mg_3Zn_3Y_2$	39.6	33.7	26.7	-
G	5	Mg_3Zn_6Y	32.4	57.5	10.1	-
H	5	MgZnCu	34.9	31.6	-	32.5

and 3g. According to SAED patterns (Fig. 3f and 3h), the particles in Fig.3e and 3g can be identified as $Mg_3Zn_3Y_2$ phase and Mg_3Zn_6Y phase, respectively.

2.2 Immersion test

2.2.1 Hydrogen and mass loss

The hydrogen evolution of the Mg-3Zn-1Y-*x*Cu (x=0, 1, 3, 5) alloys immersed in 3.5wt% NaCl solution for 72 h is shown in Fig.4a. Mg-3Zn-1Y alloy generates the least hydrogen, and the hydrogen evolution volume of Cu-containing alloys is increased significantly with the increase in Cu content. The Mg-3Zn-1Y-5Cu alloy generates the most hydrogen with hydrogen evolution volume of 619.88 mL. Fig.4b depicts the mass loss rate of Mg-3Zn-1Y-*x*Cu (x=0, 1, 3, 5) alloys. The Mg-3Zn-1Y alloy presents the lowest mass loss rate of 0.25 $mg\cdot cm^{-1}\cdot h^{-1}$. Notably, the mass loss rate of the Mg-3Zn-1Y alloy is signifi-

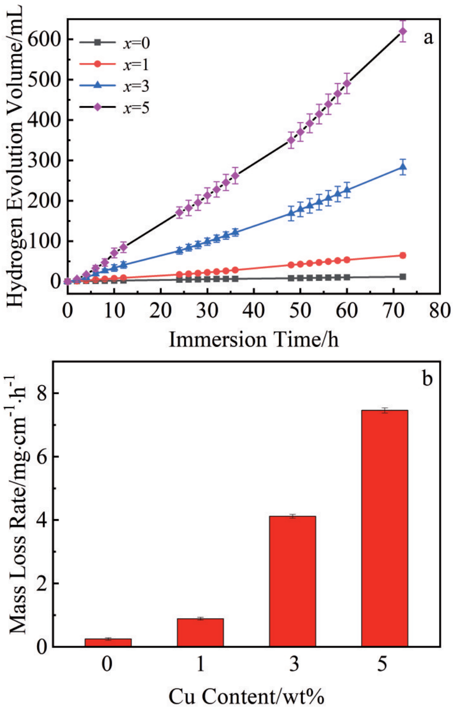

Fig.4 Immersion test results of Mg-3Zn-1Y-*x*Cu (*x*=0, 1, 3, 5) alloys in 3.5wt% NaCl solution at 25 °C: (a) hydrogen evolution volume and (b) mass loss rate

cantly increased by Cu addition. Surprisingly, the mass loss rate of Mg-3Zn-1Y-5Cu alloy is about 30 times higher than that of Mg-3Zn-1Y alloy. Thus, it can be inferred that the increasing volume fraction of MgZnCu phase does significantly accelerate the corrosion rate of Mg-3Zn-1Y-*x*Cu alloys.

2.2.2 Corrosion morphology characterization

The surface evolution of Mg-3Zn-1Y-*x*Cu (*x*=0, 1, 3, 5) alloys after immersion in 3.5wt% NaCl solution at 25 °C is presented in Fig.5. Overall, the corrosion process of the Mg-3Zn-1Y-*x*Cu alloys is significantly accelerated with the increase in Cu content. After immersion for 10 min, the surface of Mg-3Zn-1Y-1Cu alloy becomes dark due to formed oxidation film and a few initiation sites for pitting corrosion can be observed. There is no significant color change on the Mg-3Zn-1Y-3Cu alloy surface, but more severe pitting corrosion can be observed, compared with Mg-3Zn-1Y-1Cu alloy. Additionally, for the Mg-3Zn-1Y-5Cu alloy, its surface is completely corroded, forming a large number of corrosion pits. After immersion for 30 min, a large number of pits are aligned, the corroded area is increased with the increase in Cu content from 1wt% to 3wt%, and loose corrosion products are piled up on the Mg-3Zn-1Y-5Cu alloy surface. The surface of Mg-3Zn-1Y alloy barely has small dark area after immersion for 30 min due to its uniform oxidation film, and pitting can hardly be observed after immersion for 60 min.

SEM images of the corrosion film on Mg-3Zn-1Y-*x*Cu (*x*=0, 1, 3, 5) alloys after immersion in 3.5wt% NaCl solution for 2 h are shown in Fig.6. It can be seen that the alloys exhibit different types of surface morphologies. As for the Mg-3Zn-1Y alloy, most area is covered by corrosion products (Fig.6a). As shown in Fig.6b, the corrosion product in some areas is dense and flat with irregular grain coverage. In contrast, the

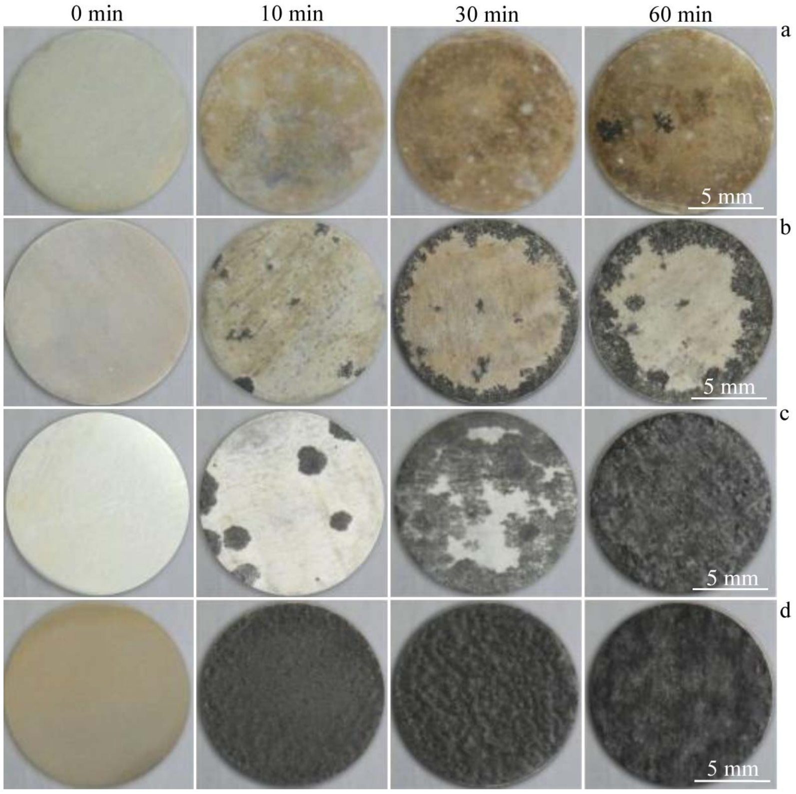

Fig.5 Surface evolution of Mg-3Zn-1Y-*x*Cu alloys after immersion in 3.5wt% NaCl solution at 25 °C: (a) *x*=0, (b) *x*=1, (c) *x*=3, and (d) *x*=5

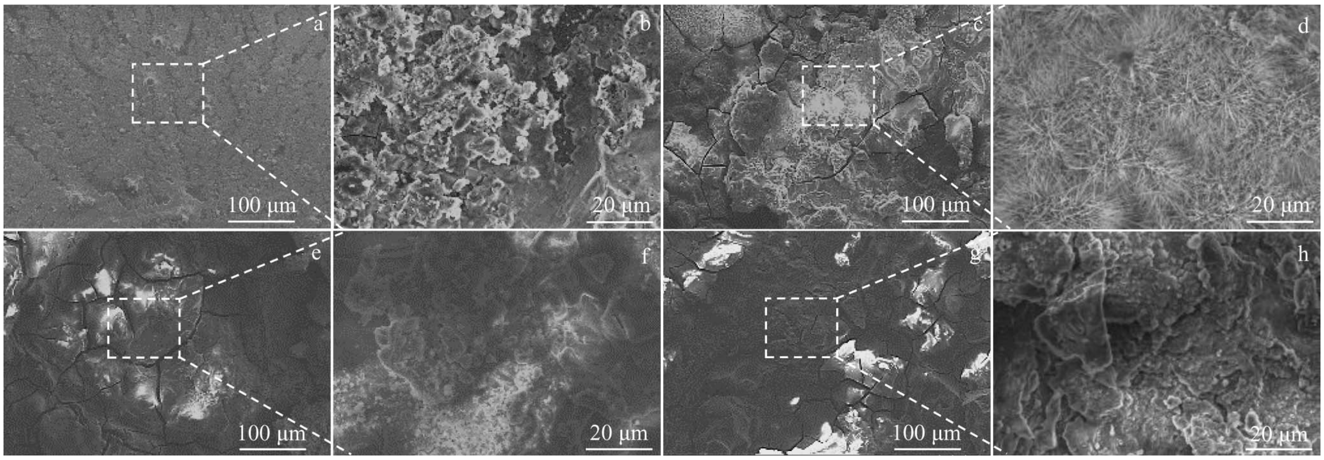

Fig.6 SEM images of corrosion film on Mg-3Zn-1Y-xCu alloys after immersion in 3.5wt% NaCl solution at 25 °C for 2 h: (a–b) x=0, (c–d) x=1, (e–f) x=3, and (g–h) x=5

surface of Mg-3Zn-1Y-1Cu alloy is completely covered by corrosion product layer with corrosion cracks (Fig. 6c), and needle-like structures can be observed on the Mg-3Zn-1Y-1Cu surface (Fig. 6d). More and more corrosion products with obvious corrosion crack are accumulated on the Mg-3Zn-1Y-3Cu alloy surface, as shown in Fig. 6e. The accumulation of loose irregular particles on the surface indicates that the corrosion product film does not provide a good physical barrier (Fig. 6f). The corrosion product layer on the surface of Mg-3Zn-1Y-5Cu alloy is more uneven and much looser (Fig. 6g–6h) than that of Mg-3Zn-1Y-3Cu alloy. These results all confirm that the Cu addition can significantly damage the integrity and compactness of the corrosion product film.

To investigate the corrosion behaviour, SEM cross-section morphologies of the corrosion products are presented in Fig. 7. The corrosion product film of the Mg-3Zn-1Y-xCu (x=0, 1, 3, 5) alloys shows different cross-section morphologies and film thicknesses. It can be found that the thicknesses are increased with the increase in Cu content. For the Mg-3Zn-1Y and Mg-3Zn-1Y-1Cu alloys, the corrosion layer formed on the surface is compact and quite homogeneous (Fig. 7a – 7b). Besides, the corrosion layer of Mg-3Zn-1Y-1Cu alloy is thicker (3 – 5 μm) than that of Mg-3Zn-1Y alloy (2–3 μm). When the Cu content is 3 wt%, an inhomogeneous and loose corrosion layer with average thickness of 6 – 9 μm can be observed (Fig. 7c). After alloying with 5 wt% Cu, the corrosion attack becomes more obvious, compared with other alloys, and a small number of cracks can be observed in corrosion layer with average thickness of 20 – 50 μm (Fig. 7d). Although Mg-3Zn-1Y-5Cu alloy has the thickest surface corrosion product layer, its protection is the worst because of its loose surface and numerous cracks[24–25].

EDS analysis results of corrosion products marked in Fig. 7 are shown in Table 2. It can be found that the corrosion pro-

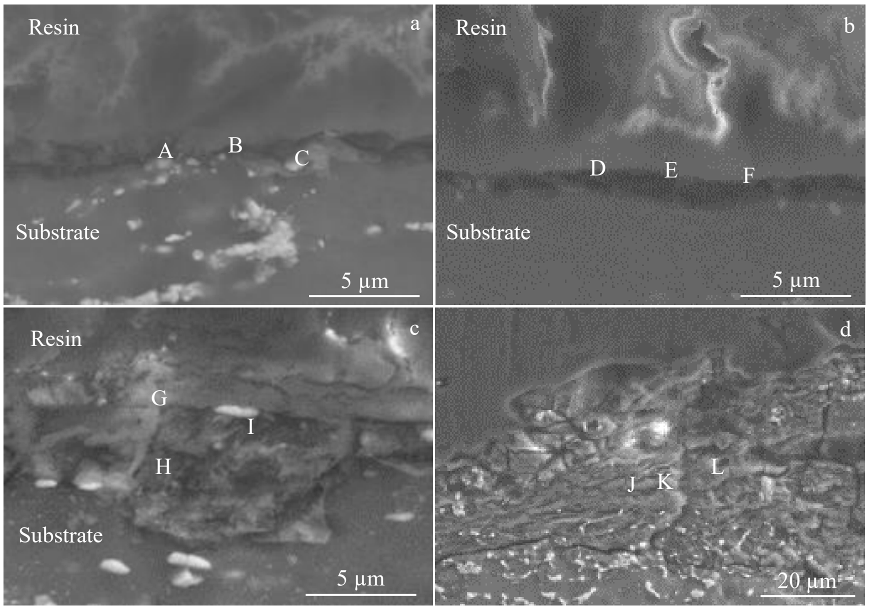

Fig.7 SEM cross-section morphologies of Mg-3Zn-1Y-xCu alloys after immersion in 3.5wt% NaCl solution at 25 °C for 2 h: (a) x=0, (b) x=1, (c) x=3, and (d) x=5

duct is $Mg(OH)_2$ since the atomic ratio of Mg to O is 1:2. In contrast, the Mg/O ratios at other positions are different, which indicates that the corrosion products have inhomogeneous composition. The Mg/O ratio of approximately 1 indicates the presence of MgO, and that between 0.5 and 1 may result from the limited analytical accuracy of EDS or the transformation from hydroxide to oxide. For Mg-3Zn-1Y-3Cu and Mg-3Zn-1Y-5Cu alloys, the second phase particles can also be observed in the corroded areas and uncorroded matrix, indicating that some second phase particles are not dissolved. Furthermore, the undissolved particles in the corroded areas are probably Mg_3Zn_6Y phase, because the Zn/Y atomic ratio is 5.8.

In order to determine the composition of corrosion products, the corrosion product film on the Mg-3Zn-1Y-5Cu alloy is detected by depth profiling through XPS. Fig. 8 presents XPS spectra of Mg 1s, Zn 2p, Y 3d, and Cu 2p before and after sputtering with the depth of 500 μm, and the bonding energies of related element spectra are listed in Table 3. Mg 1s spectrum of the as-received sample (Fig. 8a) can be divided into two peaks of $Mg(OH)_2$ and $MgCO_3$, whereas the as-sputtered sample contains three peaks of $Mg(OH)_2$, MgO, and $MgCO_3$. The detected $MgCO_3$ in the inner layer of the corrosion products may be derived from loose and cracked corrosion products (Fig. 6h), facilitating the diffusion of CO_2[30]. The Zn 2p, Y 3d, and Cu 2p peaks can hardly be detected in the as-received sample, but can be found in the as-sputtered sample. The Zn 2p and Y 3d peaks are linked to ZnO and Y_2O_3, respectively, and Cu 2p peak can be assigned to $Cu(OH)_2$ and CuO in the corrosion products. It can be concluded that the inner layer is mainly composed of $Mg(OH)_2$, MgO, $MgCO_3$, and a small number of other oxides, and the surface layer consists of $Mg(OH)_2$ and $MgCO_3$ species. Similar results are obtained in Mg-Zn and Mg-Al alloys[31–32].

Table 2 EDS analysis results of corrosion products marked in Fig.7

Location	x	Element content/at%				
		O	Mg	Zn	Y	Cu
A	0	67.29	32.30	-	0.41	-
B	0	63.95	34.78	0.64	0.63	-
C	0	67.04	32.69	-	0.27	
D	1	46.48	50.30	0.85	0.79	1.58
E	1	62.78	35.45	0.45	0.32	0.99
F	1	69.68	29.84	0.35	0.07	0.06
G	3	47.71	50.11	0.90	0.57	0.71
H	3	58.49	30.07	0.88	0.10	1.45
I	3	55.50	44.28	-	0.07	0.15
J	5	59.45	39.21	0.75	0.10	0.49
K	5	58.64	40.37	0.51	0.11	0.37
L	5	2.71	51.55	38.92	6.76	0.06

2.3 Electrochemical measurements

2.3.1 OCP analysis

Fig. 9 presents OCP variations of Mg-3Zn-1Y-xCu (x=0, 1, 3, 5) alloys during immersion in 3.5wt% NaCl solution. OCPs

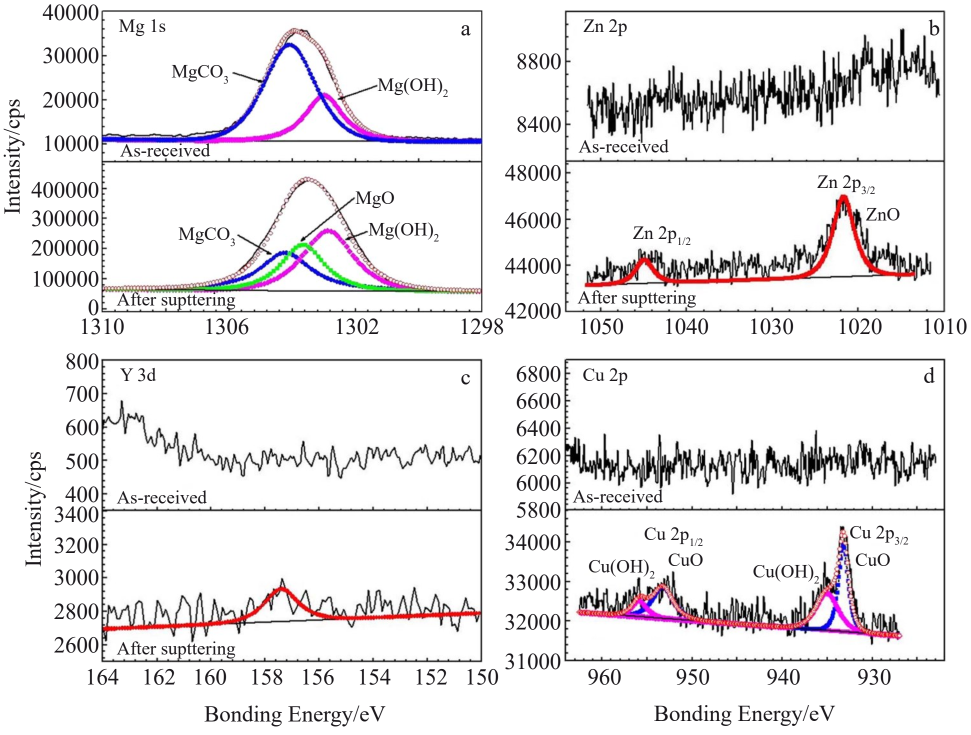

Fig.8 XPS spectra of corrosion products of Mg-3Zn-1Y-5Cu alloy after immersion in 3.5wt% NaCl solution for 2 h: (a) Mg 1s, (b) Zn 2p, (c) Y 3d, and (d) Cu 2p

Table 3 Bonding energies of related element spectra and compounds

Element spectrum	Bonding energy/eV	Component	Ref.
Mg 1s	1304.80	$MgCO_3$	[26]
	1303.90	MgO	[26]
	1302.70	$Mg(OH)_2$	[26]
Zn 2p	1045.3 ($2p_{2/3}$)	ZnO	[27]
Y 3d	156.6	Y_2O_3	[28]
Cu 2p	935.2 ($2p_{2/3}$)	$Cu(OH)_2$	[29]
	933.1 ($2p_{2/3}$)	CuO	[29]

are very different at the beginning stage and gradually become stable within 30 min. OCPs of Mg-3Zn-1Y and Mg-3Zn-1Y-1Cu alloys are increased slowly with immersion time at the first stage, whereas that of Mg-3Zn-1Y-3Cu alloy is increased rapidly and then decreased. The potentials of Mg-3Zn-1Y, Mg-3Zn-1Y-1Cu, and Mg-3Zn-1Y-3Cu alloys become stable after immersion for about 972, 283, and 250 s, respectively. In contrast, OCP of Mg-3Zn-1Y-5Cu alloy slightly decreases at the beginning, and it does not become steady even after 60 min. The relatively stable OCP of Mg-3Zn-1Y alloy is more negative than that of other Cu-containing alloys.

OCP variations are related to the formation and dissolution of the surface film on the alloys[33–34]. The relatively stable OCP reflects the dynamic balance between the formation and dissolution of the corrosion products. The increasing and reducing process of the potential may be ascribed to the formation of the oxidation film and dissolution of Mg[35–36]. In addition, the relatively stable OCP of Mg-3Zn-1Y alloy is more negative than that of other Cu-containing alloys. The OCP values tend to increase with the increase in Cu content, indicating the increased surface activation of the Mg-3Zn-1Y-*x*Cu alloys.

2.3.2 Polarization curves

Fig. 10 presents the polarization curves of Mg-3Zn-1Y-*x*Cu (*x*=0, 1, 3, 5) alloys in 3.5wt% NaCl solution. The anodic branches of the polarization curves are much steeper than the cathodic branches, indicating that the corrosion of Mg-3Zn-1Y-*x*Cu alloys is controlled by the cathode hydrogen evolution reaction ($2H_2O+2e^-\rightarrow H_2+2OH^-$) [37–38]. In consideration of the complicated polarization behaviour of Mg alloys due to the negative difference effect[36,39], the corrosion current densities at the free corrosion potentials of the cathodic branches from the polarization curves are simply fitted by Tafel extrapolation method, and the results are listed in Table 4. At the cathodic branch, Tafel slope is decreased with the increase in Cu content.

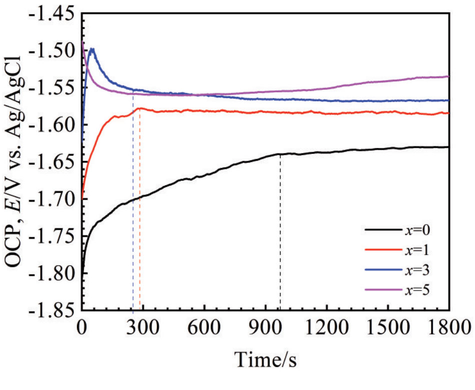

Fig.9 OCP variations of Mg-3Zn-1Y-*x*Cu (*x*=0, 1, 3, 5) alloys during immersion in 3.5wt% NaCl solution

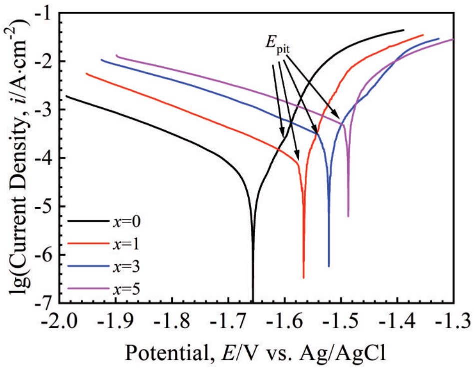

Fig.10 Polarization curves of hot-rolled Mg-3Zn-1Y-*x*Cu (*x*=0, 1, 3, 5) alloys in 3.5wt% NaCl solution

The corrosion potential (E_{corr}) of Mg-3Zn-1Y, Mg-3Zn-1Y-1Cu, Mg-3Zn-1Y-3Cu, and Mg-3Zn-1Y-5Cu alloys is −1.657, −1.566, −1.522, and −1.486 V vs. Ag/AgCl, respectively. Compared with Mg-3Zn-1Y alloy, the Cu-containing alloys show more positive corrosion potentials. Furthermore, the corrosion potential of alloy shifts towards the positive direction with the increase in Cu content. This phenomenon is also reported in other Mg alloys[40–42]. Additionally, the pitting potential (E_{pit}) of Mg-3Zn-1Y alloy (−1.595 V) appears in the anode polarization curve, whereas E_{pit} of Cu-containing alloys appears in the cathodic curves, and E_{pit} is lower than E_{corr}. This result is reported in the pure Mg, AZ91 alloy, and Mg-Al-Gd alloy[36,43–44]. This phenomenon indicates that the sample has been corroded even when the measured potential is lower than the corrosion potential, because the corrosion product film of Cu-containing alloys is not protective in the corrosive medium[36].

The corrosion current densities of the Mg-3Zn-1Y-*x*Cu (*x*=0, 1, 3, 5) alloys are increased with the addition of Cu element, and the Mg-3Zn-1Y-5Cu alloy exhibits the highest i_{corr}. Therefore, the cathodic reaction is easier for the Mg-3Zn-1Y-5Cu alloy than that for the other three alloys. The order of degradation rate from slow to fast is as follows: Mg-3Zn-1Y<

Table 4 Fitting results of polarization curves of Mg-3Zn-1Y-*x*Cu (*x*=0, 1, 3, 5) alloys

x	E_{corr}/V vs. Ag/AgCl	E_{pit}/V vs. Ag/AgCl	i_{corr}/μA·cm^{-2}
0	−1.657±0.006	−1.595±0.005	70.31±13.1
1	−1.566±0.005	−1.576±0.004	112.3±15.2
3	−1.522±0.006	−1.540±0.005	311.7±16.3
5	−1.486±0.004	−1.495±0.004	638.3±20.3

Mg-3Zn-1Y-1Cu<Mg-3Zn-1Y-3Cu<Mg-3Zn-1Y-5Cu. Thus, it is further proved that the higher the Cu content, the worse the corrosion resistance of Mg-3Zn-1Y-*x*Cu alloys.

2.3.3 EIS analysis

To further investigate the corrosion behaviour of Mg-3Zn-1Y-*x*Cu (*x*=0, 1, 3, 5) alloys, EIS tests were conducted in 3.5wt% NaCl solution. Different Nyquist plots are shown in Fig. 11a, and it is revealed that the Mg-3Zn-1Y-*x*Cu alloys have different electrochemical corrosion mechanisms. The Nyquist plots of the Mg-3Zn-1Y and Mg-3Zn-1Y-1Cu alloys consist of two capacitance loops and one inductance loop. The two capacitance loops are attributed to the existence of the protective films on their surface[33,45]. The inductive loop is ascribed to the high concentration of Mg^{2+} on the relatively film-free areas[46–47] or the intermediate surface adsorption step during the corrosion process[48]. In contrast, the Nyquist plots of Mg-3Zn-1Y-3Cu and Mg-3Zn-1Y-5Cu alloys vary greatly. The second capacitance loop disappears and a large inductance loop can be observed. The disappearance of medium frequency capacitance loop indicates that the corrosion product film is degraded completely in a short time[49]. The existence of inductance loop indicates that the Mg matrix suffers corrosion attack. The Bode impedance plots are shown in Fig. 11b, and it is found that the impedance values of Mg-3Zn-1Y-*x*Cu alloys are quickly decreased with the increase in Cu content, implying that the alloying with Cu element results in the rapid failure of the surface film. According to the Bode phase angle plots (Fig. 11b), two wave crests and one trough can be observed for the Mg-3Zn-1Y and Mg-3Zn-1Y-1Cu alloys, implying the existence of three time constants. However, there are one wave crest and one trough in the Bode phase angle plots of Mg-3Zn-1Y-3Cu and Mg-3Zn-1Y-5Cu alloys, suggesting the existence of two time constants.

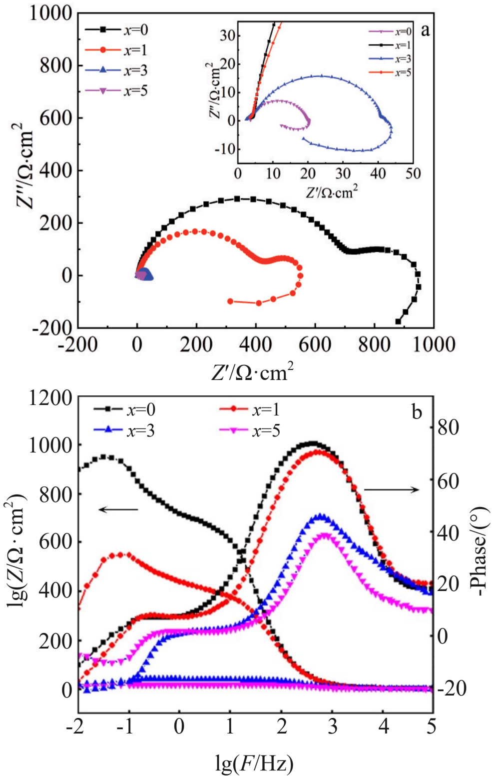

Fig.11 EIS results of hot-rolled Mg-3Zn-1Y-*x*Cu (*x*=0, 1, 3, 5) alloys in 3.5wt% NaCl solution: (a) Nyquist plots; (b) Bode impedance plots and phase plots

EIS results of Mg-3Zn-1Y-*x*Cu (*x*=0, 1, 3, 5) alloys are fitted using the equivalent circuits, as shown in Fig. 12. R_s, R_t, and R_f represent the solution resistance, charge transfer resistance, and resistance of corrosion products, respectively. R_L and L are the inductance resistance and inductance, respectively. CPE_f and CPE_{dl} are constant phase element related with the corrosion product film and electric double layer, and they are denoted as Y and n, respectively. Generally, R_t values reflect the dissolution rates of Mg matrix[50]. The lower the R_t value, the faster the dissolution rate. According to the fitting results in Table 5, Mg-3Zn-1Y alloy shows the largest R_t value (677.70 Ω·cm²), followed by Mg-3Zn-1Y-1Cu (397.40 Ω·cm²), Mg-3Zn-1Y-3Cu (40.59 Ω·cm²), and Mg-3Zn-1Y-5Cu (16.28 Ω·cm²) alloys. This result indicates that Mg-3Zn-1Y alloy possesses the best corrosion resistance and the corrosion resistance of Mg-3Zn-1Y-*x*Cu alloys deteriorates with the increase in Cu content. The result sufficiently agrees with the polarization curve and immersion test results. The R_f value of the Mg-3Zn-1Y-1Cu alloy is lower than that of the Mg-3Zn-1Y alloy by about 70 Ω·cm², which confirms that the protective ability of oxide film is weakened due to the addition of Cu. Moreover, R_L value of Mg-3Zn-1Y-*x*Cu alloys is dramatically reduced with the increase in Cu content, implying the increasing tendency of pitting corrosion. The R_L value of the Mg-3Zn-1Y-1Cu alloy reduces by 1.3 times, compared with that for Mg-3Zn-1Y alloy, and the reduction ratio is 32 and 41 times for the Mg-3Zn-1Y-3Cu and for Mg-3Zn-1Y-5Cu alloys, respectively.

3 Discussion

The deteriorated corrosion resistance of Mg-3Zn-1Y-*x*Cu (*x* =0, 1, 3, 5) alloys is proved by the electrochemical and immersion results, which can be attributed to the effect of Cu addition on the microstructure and corrosion product film.

3.1 Effect of Cu on micro-galvanic corrosion of Mg-3Zn-1Y alloy

For the Mg-3Zn-1Y alloy, the Mg_3Zn_6Y phase is the exclusive second phase and its electrode potential is much higher than that of *α*-Mg matrix[51], because the standard electrode potential of Zn (−0.76 V) is higher than that of *α*-Mg and that of Y (−2.37 V) is equal to that of *α*-Mg (−2.37 V).

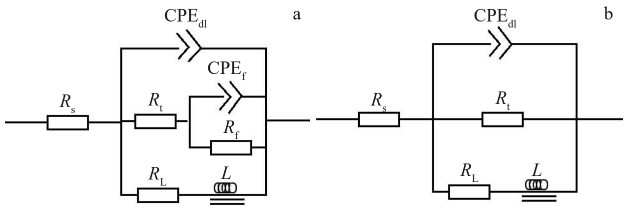

Fig.12 Equivalent circuits of EIS results for hot-rolled Mg-3Zn-1Y-*x*Cu (*x*=0, 1, 3, 5) alloys: (a) *x*=0 and 1; (b) *x*=3 and 5

Table 5 Fitting parameters of EIS analysis results of Mg-3Zn-1Y-*x*Cu (*x*=0, 1, 3, 5) alloys

Parameter	x=0	x=1	x=3	x=5
$R_s/\Omega\cdot cm^2$	4.102	3.696	3.028	3.605
$Y_0/\times10^{-5}\ \Omega^{-1}\cdot cm^{-2}\cdot s^{-1}$	1.46	1.68	5.49	8.20
n	0.923	0.923	0.845	0.882
$R_t/\Omega\cdot cm^2$	677.70	397.40	40.59	16.28
$Y_f/\times10^{-3}\ \Omega^{-1}\cdot cm^{-2}\cdot s^{-1}$	3.04	4.67	-	-
n_f	0.783	0.728	-	-
$R_f/\Omega\cdot cm^2$	291.8	222.7	-	-
$L/H\cdot cm^{-2}$	527 94	858 1	176.8	134.7
$R_L/\Omega\cdot cm^2$	877.4	634.1	27.17	21.15

Due to the large potential difference between *α*-Mg and Mg_3Zn_6Y phases, the *α*-Mg matrix adjacent to the Mg_3Zn_6Y phase preferentially dissolves as a micro-anode, whereas the central region of the *α*-Mg matrix is almost uneroded.

For the Cu-containing alloys, MgZnCu phase is the main second phase. The MgZnCu phase has a high potential, resulting from the positive standard electrode potential of Cu (+0.34 V) and relatively higher standard electrode potential of Zn (−0.76 V), compared with those of Mg and Y. According to Ref. [51 – 53], the potential difference between the second phase and *α*-Mg matrix is ranked in a decreasing order as MgZnCu (680 mV) >$Mg_3Zn_3Y_2$ (530 mV) >Mg_3Zn_6Y (220 mV). The large potential difference between the anode (*α*-Mg) and the cathode (MgZnCu phase) is bound to the rapid initiation and efficient reaction of galvanic corrosion. Additionally, MgZnCu phase of Cu-containing alloys accelerates the kinetics process of micro-galvanic corrosion, which is confirmed by the relatively higher cathodic current and smaller Tafel slope, compared with those of Mg-3Zn-1Y alloy (Fig. 10). This change in cathode dynamics may significantly impair the corrosion performance of the Cu-containing alloys during the cathode-control process.

For the Mg-3Zn-1Y-3Cu and Mg-3Zn-1Y-5Cu alloys, the second phase contains MgZnCu, Mg_3Zn_6Y, and $Mg_3Zn_3Y_2$ phases. Micro-galvanic corrosion also occurs at the MgZnY (Mg_3Zn_6Y and $Mg_3Zn_3Y_2$)/MgZnCu interface. The MgZnY phase serves as anode to adjacent MgZnCu phase, resulting in the preferential corrosion of MgZnY phase, which also promotes pitting corrosion. Furthermore, pitting also occurs inside the *α*-Mg grain owing to the micro-galvanic corrosion between *α*-Mg and the second phase. In fact, the quantity of MgZnCu phase in Mg-3Zn-1Y-5Cu alloy is the most, and that in Mg-3Zn-1Y-1Cu alloy is the least. A large number of MgZnCu particles aggravate the pitting corrosion of *α*-Mg phase, which may be the reason why Mg-3Zn-1Y-5Cu alloy has the smallest R_L value.

3.2 Effect of Cu on corrosion film of Mg-Zn-Y alloy

It is known that the protection performance of corrosion product film also plays an important role in the corrosion resistance of Mg-Zn-Y alloys. The protection effect of corrosion products is mainly determined by the solubility and Pilling Bedworth ratio (PBR)[54–55]. The effect of solubility on the corrosion is negligible, because all corrosion products have low solubility, as listed in Table 6. The compactness of corrosion product film can be elaborated by PBR, which is mathematically expressed by Eq.(1)[54], as folows:

$$\mathrm{PBR} = \frac{V_{\mathrm{com}}}{V_{\mathrm{M}}} = \frac{M_{\mathrm{com}}\rho_{\mathrm{M}}}{nA\rho_{\mathrm{com}}} \tag{1}$$

where V_{com} and ρ_{com} are the compound volume and density, respectively; V_m and ρ_M are the metal volume and density, respectively; M_{com} and A are the molar mass and atomic mass of the compounds and the metal, respectively; n is the number of metal atoms in the compounds.

The calculated PBR values are shown in Table 7. Usually, PBR is representative of the stress state of the corrosion product film. Generally, when 1<PBR<2, a certain degree of compressive stress exists in the surface film, suggesting denser and more protective film. When PBR<1 or PBR>2, the surface film produces tensile stress or the excessive compressive stress is produced, resulting in the film cracking and spalling.

According to the calculated results in Table 7, PBR of all compounds is increased with the increase in Cu content. $Mg(OH)_2$ is the main corrosion product and its PBR directly affects the protection performance of the corrosion product film. Interestingly, the calculated PBR of $Mg(OH)_2$ in the Mg-3Zn-1Y and Mg-3Zn-1Y-1Cu alloys ranges from 1.88 to 1.96, whereas that in the Mg-3Zn-1Y-3Cu and Mg-3Zn-1Y-5Cu alloys is 2.04 – 2.10, which are larger than 2. Since the PBR value of $Mg(OH)_2$ is greater than 2, the film crack suffers excessive compressive stress, leading to the reduced protection effect. Therefore, the highest R_f value (291.8

Table 6 Solubility of related compounds in Mg-3Zn-1Y-*x*Cu (*x*= 0, 1, 3, 5) alloys at 20 °C (mg·g⁻¹)

Compound	Solubility
MgO	8.6×10^{-2}
$Mg(OH)_2$	9.6×10^{-3}
$MgCO_3$	3.9×10^{-1}
ZnO	1.6×10^{-2}
Y_2O_3	-
CuO	-
$Cu(OH)_2$	1.7×10^{-5}

Table 7 PBRs of related compounds in Mg-3Zn-1Y-*x*Cu (*x*=0, 1, 3, 5) alloys

Compound	x=0	x=1	x=3	x=5
MgO	0.86	0.89	0.93	0.96
$Mg(OH)_2$	1.88	1.96	2.04	2.10
$MgCO_3$	2.14	2.24	2.32	2.40
ZnO	1.11	1.16	1.20	1.24
Y_2O_3	1.72	1.80	1.86	1.92
CuO	-	0.91	0.94	0.98
$Cu(OH)_2$	-	2.31	2.39	2.47

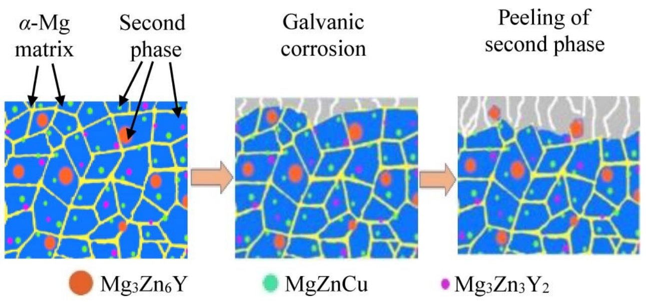

Fig.13 Schematic diagram of corrosion mechanism of Mg-3Zn-1Y-5Cu alloy

Ω·cm^2) and the flat corrosion morphology (Fig.6a) of Mg-3Zn-1Y alloy are mainly attributed to the moderate PBR values of $Mg(OH)_2$, ZnO, and Y_2O_3. Except for ZnO and Y_2O_3, the PBR values of corrosion products in Mg-3Zn-1Y-5Cu alloy are between 1 and 2, exhibiting the lowest protective effect.

3.3 Corrosion mechanism

Based on the above analysis, a possible corrosion mechanism of Mg-3Zn-1Y-5Cu alloy is proposed, and the corresponding schematic diagram is shown in Fig. 13. When 5wt% Cu is added into the Mg-3Zn-1Y alloy, the MgZnCu phase can be formed as the main second phase, which is distributed both in the matrix and along grain boundary. When Mg-3Zn-1Y-5Cu alloy samples are exposed to the NaCl solution, MgZnCu phase acting as the cathode drives the rapid dissolution of Mg matrix via the micro-galvanic corrosion[35,56]. Subsequently, insoluble $Mg(OH)_2$ is formed and deposited on the surface. Moreover, the OH^- bonds with M^{n+} (metal anodic ion) from the anodic reaction ($M \rightarrow M^{n+} + ne^-$) to form hydroxides of Zn, Y, and Cu. The hydroxides can be partially or completely converted to stable oxides. Despite the formation of corrosion film, more and more matrix is exposed to the corrosive medium[57] due to cracks in the film. Finally, the corrosion occurs into the interior of alloy. The cracks accelerate the corrosive medium diffusion and aggravate the corrosion of Mg-3Zn-1Y-5Cu alloy. With the corrosion proceeding, such inward corrosion aggravates the dissolution of α-Mg matrix, leading to the peeling of the second phase.

4 Conclusions

1) The hot-rolled Mg-3Zn-1Y-xCu (x=0, 1, 3, 5) alloys mainly consist of α-Mg and Mg_3Zn_6Y phases. The content of MgZnCu phase depends on the amount of Cu element. The grain size of the alloys decreases slightly after Cu addition, but it does not change significantly with the further increase in Cu content.

2) The added Cu significantly deteriorates the compactness of corrosion products on the Mg-3Zn-1Y-xCu alloy surface. The formed corrosion product films are mainly composed of magnesium hydroxides/oxides and a small number of other oxides.

3) The added Cu deteriorates the corrosion resistance of Mg-3Zn-1Y alloy. The corrosion rate of Mg-3Zn-1Y-xCu alloys is increased significantly with the increase in Cu content. The decrease in corrosion resistance of the alloy can be attributed to the accelerated galvanic corrosion of the MgZnCu phase with high electrode potential and the degraded compactness of corrosion product film.

References

1 Jo S, Lee G M, Lee J U *et al. Journal of Magnesium and Alloys*[J], 2024, 12(2): 779
2 Zhang Y Z, Chen X T, Zhang S H *et al. Materials Letters*[J], 2024, 358: 135751
3 Li Y R, Wu Z, Wei J L. *Vacuum*[J], 2023, 218: 112663
4 Wang Yuecun, Zhou Fan, Ge Yanfeng *et al. Materials China*[J], 2020, 39(2): 100 (in Chinese)
5 Hanawalt J D, Nelson C E, Peloubet J A. *Transaction of American Institute of Mining, Metallurgical, and Petroleum Engineers*[J], 1942, 147: 273
6 Zhang C, Wu L, Huang G S *et al. Journal of Materials Science and Technology*[J], 2019, 35(9): 2086
7 Liu M, Uggowitzer P J, Nagasekhar A V *et al. Corrosion Science*[J], 2009, 51(3): 602
8 Zhu H M, Sha G, Liu J W *et al. Journal of Alloys and Compounds*[J], 2011, 509(8): 3526
9 Zhu S Z, Luo T J, Zhang T A *et al. Materials Science and Engineering A*[J], 2017, 689: 203
10 Geng Z W, Xiao D H, Chen L. *Journal of Alloys and Compounds*[J], 2016, 686: 145
11 Liu B S, Yang Y X, Zhang Y Z *et al. Journal of Physical and Chemistry of Solids*[J], 2020, 144: 109
12 Lotfpour M, Emamy M, Dehghanian C *et al. Journal of Materials Engineering and Performance*[J], 2017, 26: 2136
13 Zhou M, Liu C M, Xu S Y *et al. Materials and Corrosion*[J] 2018, 69(6): 760
14 Safari N, Toroghinejad M R, Kharaziha M. *Materials Chemistry and Physical*[J], 2019, 237: 121838
15 Chen L, Wu Z, Xiao D H *et al. Materials and Corrosion*[J] 2015, 66(10): 1159
16 Kawamura Y, Hayashi K, Inoue A *et al. Materials Transactions*[J], 2001, 42(7): 1172
17 Pérez P, Onofre E, Cabeza S *et al. Corrosion Science*[J], 2013, 69: 226
18 Lee J Y, Kim D H, Lim H K *et al. Materilas Letters*[J]. 2005, 59: 3801
19 Mora E, Garcés G, Oñorbe E *et al. Scripta Materilia*[J], 2009, 60(9), 776
20 Zhang Y Z, Wang X Y, Kuang Y F *et al. Materials Letters*[J], 2017, 195: 194
21 Wu X F, Xu C X, Zhang Z W *et al. Transactions of Nonferrous Metals Society of China*[J], 2023, 33(2): 422
22 Hamaya A, Horiuchi T, Oohira Y *et al. Materials Transactions*[J], 2013, 54(5): 641

23 Wang Y B, Huang Y X, Meng X C *et al*. *Journal of Alloys and Compounds*[J], 2017, 696: 875

24 Feng Y J, Wei L, Chen X B *et al*. *Corrosion Science*[J], 2019, 159: 108

25 Lei T, Tang W, Cai S H. *Corrosion Science*[J], 2012, 54: 270

26 Song Y W, Han E H, Dong K H *et al*. *Corrosion Science*[J], 2013, 72: 133

27 Li L J, Zhang Y Z, Lei J L *et al*. *Corrosion Science*[J], 2014, 85: 174

28 Chen X, Qi Z, Zhang G. *Physica B: Condensed Matter*[J], 2009, 404(1): 146

29 Yuan S J, Pehkonen S O. *Corrosion Science*[J], 2007, 49(3): 1276

30 Wang L, Shinohara T, Zhang B P. *Applied Surface Science*[J], 2010, 256(20): 5807

31 Song Y W, Han E H, Dong K H *et al*. *Corrosion Science*[J], 2014, 88: 215

32 Wang L, Zhang B P, Shinohara T. *Materials & Design*[J], 2010, 31: 857

33 Song Y W, Shan D Y, Chen R S *et al*. *Journal of Alloys and Compounds*[J], 2009, 484(1–2): 585

34 Liu M, Schmutz P, Uggowitzer P J *et al*. *Corrosion Science*[J], 2010, 52(11): 3687

35 Ha H Y, Kang J Y, Kim S G *et al*. *Corrosion Science*[J], 2014, 82: 369

36 Lu F M, Ma A B, Jiang J H *et al*. *Corrosion Science*[J], 2015, 94: 171

37 He M F, Liu L, Wu Y T *et al*. *Corrosion Science*[J], 2008, 50(12): 3267

38 Turhan M C, Li Q Q, Jha H *et al*. *Electrochimica Acta*[J], 2011, 56: 7141

39 Liu R L, Scully J R, Williams G *et al*. *Electrochimica Acta*[J], 2018, 260: 184

40 Chen J X, Peng W, Zhu L *et al*. *Materials Technology*[J], 2018, 33(2): 145

41 Yan X D, Wan P, Tan L L *et al*. *Materials Science and Engineering C*[J], 2018, 93: 565

42 Li Y, Liu L, Wan P *et al*. *Biomaterials*[J], 2016, 106: 250

43 Song G, Atrens A, Stjohn D *et al*. *Corrosion Science*[J], 1997, 39(5): 855

44 Song G, Atrens A. *Advanced Engineering Materials*[J], 2007, 9(3): 177

45 Hagihara K, Okubo M, Yamasaki M *et al*. *Corrosion Science*[J], 2016, 109: 68

46 Song Y W, Shan D Y, Chen R S *et al*. *Corrosion Science*[J], 2009, 51(5): 1087

47 Wang S D, Xu D K, Chen X B *et al*. *Corrosion Science*[J], 2015, 92: 228

48 Wu G S, Zhao Y, Zhang X M *et al*. *Corrosion Science*[J], 2013, 68: 279

49 Tong L B, Zhang Q X, Jiang Z H *et al*. *Journal of the Mechanical Behavior of Biomedical Materials*[J], 2016, 62: 57

50 Liu N, Wang J L, Wang L D *et al*. *Corrosion Science*[J], 2009, 51(6): 1328

51 Baek S M, Kim B, Park S. *Metals*[J], 2018, 8(5): 323

52 Cao X, Xu C X, Zhang Z W. *Journal of Materials Science*[J], 2021, 56: 12394

53 Cao X, Li C, Wu B *et al*. *Journal of Materials Engineering and Performance*[J], 2024, 33: 1626

54 Song Y W, Shan D Y, Chen R S *et al*. *Corrosion Science*[J], 2010, 52(5): 1830

55 Zeng R, Sun L, Zheng Y *et al*. *Corrosion Science*[J], 2014, 79: 69

56 Li C Q, Xu D K, Chen X B *et al*. *Electrochimica Acta*[J], 2018, 260: 55

57 Esmaily M, Svensson J E, Fajardo S *et al*. *Progress in Materials Science*[J], 2017, 89: 92

Cu对热轧Mg-3Zn-1Y合金微观组织和腐蚀行为的影响

张跃忠[1]，陈小亭[1]，沈 静[1]，武鹏鹏[2]，张少华[2]，刘宝胜[2]

(1. 太原科技大学 化学工程与技术学院，山西 太原 030024)

(2. 太原科技大学 材料科学与工程学院，山西 太原 030024)

摘 要：研究了热轧Mg-3Zn-1Y-*x*Cu合金（*x*=0、1、3、5，质量分数）的微观组织和腐蚀行为。结果表明，Mg-3Zn-1Y-*x*Cu合金主要包含了α-Mg和Mg_3Zn_6Y相。添加Cu元素后，合金出现了MgZnCu相，并且MgZnCu相的含量随着Cu含量的增加而增加。电化学和浸泡试验结果表明，添加Cu后Mg-3Zn-1Y-*x*Cu合金的耐腐蚀性能下降，这是因为受到了合金微观组织和腐蚀产物膜性能的影响。具有高电化学电势的MgZnCu相作为强阴极加速了微电偶腐蚀。腐蚀产物膜防护性能的下降源于相应化合物PBR值的改变。

关键词：腐蚀行为；镁合金；微观组织；MgZnCu相；腐蚀产物

作者简介：张跃忠，男，1986年生，博士，副教授，太原科技大学化学工程与技术学院，山西 太原 030027，电话：0351-6988186，E-mail：yuezhongzhang@tyust.edu.cn